ZZ Freedom in Two-Qubit Gates

Xuexin Xu[1,2,3,*] and M.H. Ansari[1,2,3]

[1]*Institute for Quantum Information, RWTH Aachen University, D-52056 Aachen, Germany*

[2]*Peter Grünberg Institute, Forschungszentrum Jülich, Jülich 52428, Germany*

[3]*Jülich-Aachen Research Alliance (JARA), Fundamentals of Future Information Technologies, Jülich 52428, Germany*

Superconducting qubits on a circuit exhibit an always-on state-dependent phase error. This error is due to sub-MHz parasitic interaction that repels computational levels from noncomputational ones. We study a general theory to evaluate the "static" repulsion between seemingly idle qubits as well as the "dynamical" repulsion between entangled qubits under microwave driving gate. By combining qubits of either the same or opposite anharmonicity signs we find the characteristics of static and dynamical *ZZ* freedoms. The latter universally eliminate the parasitic repulsion, leading us to mitigate high-fidelity gate operation. Our theory introduces the opportunities for making perfect entangled and unentangled states, which is extremely useful for quantum technology.

I. INTRODUCTION

High-performance quantum processors require improvements in the fidelity of quantum logic gates. Such improvements provide opportunities for near-term quantum systems to demonstrate multipartite entanglement [1,2] and full-fledged quantum error correction for surpassing classical computer power [3,4]. These milestones can be achieved with the advent of long coherence qubits that can quickly go from perfect isolated state to strongly interacting entanglement and vice versa, using programmable electronics [5–7]. In the last decade many advances have taken place to suppress degrading interactions among qubits as well as between a qubit and environmental noise and quasiparticles [8–13]. However state-of-the-art quantum systems are yet far from being perfect [14].

In today's quantum processors single-qubit rotation is fast and precise, however two-qubit entanglement is yet to achieve a high contrast on-off operation with logical error rates below error-correction threshold [15–18]. A pair of idle qubits initialized at either $|00\rangle$ or $|11\rangle$ accumulate the phase error $\exp(i\zeta t/4)$ after time t, while $|01\rangle$ and $|10\rangle$ do it differently with the error being $\exp(-i\zeta t/4)$. Experiments show ζ is a sub-MHz coupling strength. In theory this extra force is generated due to level repulsion between computational levels, e.g., E_{11}, and noncomputational, e.g., E_{02} or E_{20} [19]. Within computational subspace this repulsion is a *ZZ* interaction, with Z being the σ_z Pauli operator, and is always internally present between any pair of qubits on

the circuit and is called *static ZZ* interaction. The effect of static *ZZ* interaction goes beyond accumulating idle phase error. Externally driven qubits by two-qubit gates produces an additional *ZZ* component on top of the static one that keeps two-qubit gates from achieving high-fidelity entanglement [20–23]. Therefore, freeing qubits from the unwanted *ZZ* interaction is highly demanded for increasing gate fidelity, which is the purpose of this paper.

In the first part we discuss Hamiltonian circuit analysis for demonstrating static *ZZ* freedom. This is better to take place first in the circuit model before fabricating the actual circuit as it requires delicate parameter tuning. We keep this part at general and self-contained as possible and indicate how all circuit parameters can impact achieving the freedom. Some of the main game players are qubit-qubit direct coupling and qubit anharmonicity values and signs. We examine several circuits with the same-sign anharmonicity, such as two transmon devices. Some of our samples are set to be similar to those tested in Refs. [24–26]. We show the possibilities for zeroing repulsion between two transmons, for example, by controlling their capacitive direct coupling. We develop our theory on circuits with opposite sign anharmonicity, such as in Ref. [19], and show under what conditions the exact *ZZ* freedom becomes possible.

In the second part we discuss another strategy for zeroing unwanted *ZZ* interaction, the *dynamical ZZ* freedom. This is applicable for circuits with built-in *ZZ* interaction, for instance, in large processors with many qubits eliminating all static *ZZ* interactions seems not to be possible. We propose to apply microwave pulses on qubits in a way

---

*x.xu@fz-juelich.de

similar to cross resonance (CR) gates [27]. The microwave pulse produces additional *ZZ* component on top of the static part and we show that for certain circuit parameters this is possible to have the two parts canceling each other, resulting in zero total *ZZ* interaction. This allows one to make perfect entanglement as well as unentanglement in the absence of parasitic interaction. Interestingly, dynamical *ZZ* freedom can be universally achieved in qubits with any anharmonicity sign.

II. GENERAL MODEL

Physical qubits have more than two energy levels and can be found in two classes (anharmonicity species): positive or negative anharmonicity. In qubits with positive (negative) anharmonicity higher levels are farther (closer) apart. A negative anharmonic qubit is transmon and an example of positively anharmonic qubit is a capacitively shunted flux qubit (CSFQ) [28]. In a single Josephson junction (JJ) transmon a rather large capacitance shunts the charging energy to warrant less sensitivity to charge fluctuations. A CSFQ, as depicted in Fig. 1(a), replaces the JJ with a closed loop of three junctions, i.e., two in-series JJ parallel to a smaller JJ (smaller in critical current and capacitance) [29,30].

A single JJ transmon can be classically characterized by the flux Φ and its canonical conjugate $Q = 2en$ being the electric charge of n Cooper pairs tunneling across the JJ, e being electron charge. The device has a periodic potential energy, i.e., $-E_J \cos(2\pi\Phi/\Phi_0)$ with the Josephson energy $E_J \equiv I_0\Phi_0/2\pi$ proportional to the critical current I_0 and the flux quantum $\Phi_0 = h/2e$, h being Planck's constant. Variables can be simplified to $\phi \equiv 2\pi\Phi/\Phi_0$ and its conjugate $n\hbar$ whose quantization can take place in the Fock space of quantum states $|m\rangle$ with $m = 0, 1, 2, \ldots$ and annihilation and creation operators $\hat{a} = \sum_m \sqrt{m}|m\rangle\langle m+1|$ and $\hat{a}^\dagger = \sum_m \sqrt{m+1}|m+1\rangle\langle m|$. Transmon canonical operators are defined $\hat{\phi} = \phi_{\mathrm{ZPF}}(\hat{a} + \hat{a}^\dagger)$ and $\hat{n} = in_{\mathrm{ZPF}}(\hat{a} - \hat{a}^\dagger)$ with the zero-point fluctuations ϕ_{ZPF} and n_{ZPF}, satisfying the minimum uncertainty $\phi_{\mathrm{ZPF}}n_{\mathrm{ZPF}} = 1/2$. The fluctuations can be determined by the characteristic impedance Z_c, i.e., $\phi_{\mathrm{ZPF}} = \sqrt{\hbar Z_c/2}$. A transmon's small anharmonicity allows approximation of the periodic potential energy in the vicinity of minimum with a fourth-degree polynomial making a Duffing oscillator, i.e., $H = \omega\hat{a}^\dagger\hat{a} + (\delta/12)(\hat{a} + \hat{a}^\dagger)^4$ with δ being anharmonicity. Higher-order corrections are known [31].

The CSFQ depicted in Fig. 1(a) has two in-series identical JJs in a closed loop with a smaller JJ that has smaller critical current αI_0 and capacitance αC_J with $\alpha < 1$. The loop carries negligible kinetic inductance and an external magnetic flux Φ_{ext} in the loop which can tune the potential energy [30]. A CSFQ potential energy is $-E_J[\cos(\phi_1 - \phi_2) + \cos(\phi_2 - \phi_3) - \alpha\cos(2\pi f - \phi_1 + \phi_3)]$ with f being $\Phi_{\mathrm{ext}}/\Phi_0$. Defining
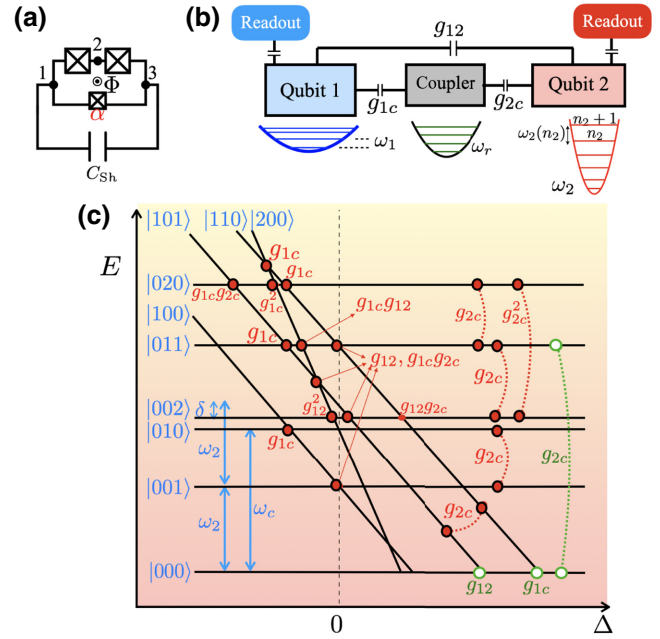

FIG. 1. (a) A CSFQ. (b) A CSFQ-transmon circuit coupled capacitively by g_{12} and via a coupler, each qubit is measured. (c) Energy diagram of a circuit with two qubits $Q1$ and $Q2$ and a resonator coupler c. Qubits have similar anharmonicity δ and frequency detuning Δ, i.e., $\omega_1 = \omega_2 - \Delta$. The plot shows how different noninteracting eigenstates $|n_{Q1}, n_c, n_{Q2}\rangle$ are coupled to one another by headed lines based on different interaction terms in Hamiltonian (1). Red head lines indicate level repulsion due to corotating terms in the interactions. White head lines indicate level repulsions by counterrotating terms.

the two variables $\phi = \phi_1 - \phi_3$ and $\phi' = \phi_1 - 2\phi_2 + \phi_3$ and working out corresponding charging energies, one can show ϕ' mode has negligible influence on the potential and can be discarded, see Appendix A. This simplifies the potential to $-E_J[2\cos(\phi/2) + \alpha\cos(2\pi f - \phi)]$. Under the condition $\alpha < 1/2$ this potential can be used as a qubit because each period conveys one minimum, not more. The potential is the most symmetric at the so-called "sweet spot" (SS), where $f = 1/2$. A less symmetric potential at $f = 1/2 + \delta f$ with $\delta f \ll 1/2 - \alpha$ has a minimum at $\phi_0 = -2\pi\alpha(\delta f)/(1/2 - \alpha)$ and in the vicinity of the minimum with phase differece $\Delta\phi = \phi - \phi_0$ it can be approximated to $(1 - 2\alpha)E_J\Delta\phi^2/4 + (\alpha - 1/8)E_J\Delta\phi^4/4! + 2\pi(\delta f)\alpha E_J(\Delta\phi - \Delta\phi^3/6)$. This potential has the simple form of a Duffing oscillator at SS, i.e., $\delta f = 0$, with the periodic frequency $\hbar\omega = \sqrt{8E_JE_C(1/2 - \alpha)}$, anharmonicity $\delta = 4E_C(\alpha - 1/8)/(1 - 2\alpha)$, and zero-point phase fluctuations $\phi_{\mathrm{ZPF}} = [4E_C/E_J(1 - 2\alpha)]^{1/4}$. In contrast to a transmon, a CSFQ with $1/8 < \alpha < 1/2$ has positive anharmonicity; see Appendix A for quantization.

A hybrid two-qubit circuit: we consider qubits $Q1$ and $Q2$ coupled via a coupler c, such as a bus resonator. Each

one of the two qubits can have positive or negative anharmonicity. In the circuit depicted in Fig. 1(b) we give an example of $Q1$ being transmon and $Q2$ being a CSFQ, however we keep this section general without referring to the qubit species. $Q1$ and $Q2$ may have small capacitive coupling g_{12} on top of indirect coupling via the coupler. The circuit Hamiltonian is

$$H = \sum_{i,n_i} \omega_i(n_i)|n_i+1\rangle\langle n_i+1|$$
$$+ \sum_{j(\neq i)} g_{ij}(\hat{a}_i + \hat{a}_i^\dagger)(\hat{a}_j + \hat{a}_j^\dagger), \quad (1)$$

with $i = 1, 2$ for qubits and c for the coupler. The energy levels in the bare basis associated to free Hamiltonian are E_{n_1} and E_{n_2} for qubits and E_{n_c} for the coupler. $\omega_i(n_i)$ is the difference between $E_{n_{i+1}}$ and E_{n_i}, therefore qubit frequencies are $\omega_{1/2}(0)$ or simply $\omega_{1/2}$. The coupler frequency ω_c is far detuned from qubits in order to warrant no backaction from the coupler on the qubit driving when external gates are applied.

Let us further analyse Hamiltonian (1). Consider a fixed frequency $Q2$ from which $Q1$ is detuned by Δ, i.e., $\omega_1 = \omega_2 - \Delta$ and similar anharmonicity δ. Given that $|n_1, n_c, n_2\rangle$ is an eigenstate for the noninteracting Hamiltonian, interaction with coupling strength $(g_{1c})^k$ provides transition to $|n_1 \pm k, n_c \mp k, n_2\rangle$, with the strength $(g_{2c})^k$ to $|n_1, n_c \mp k, n_2 \pm k\rangle$, with the strength $(g_{12})^k$ to $|n_1 \pm k, n_c, n_2 \mp k\rangle$, with the strength $g_{1c}g_{2c}$ to $|n_1 \pm 1, n_c \mp 2, n_2 \pm 1\rangle$, and so on. Figure 1(c) shows these transitions marked by corotating terms such as $\hat{a}_i\hat{a}_j^\dagger$ by red heads. The counter-rotating terms in interactions such as $\hat{a}_i\hat{a}_j$ are indicated by white heads. Each coupling is labeled by the interaction term in the Hamiltonian that is responsible for it. One can see in Fig. 1(c) that the transition between $|200\rangle$ and $|101\rangle$ takes place either by direct coupling g_{12} or via the intermediate state $|110\rangle$. In the absence of direct coupling the avoided crossing between the two levels has been found $\sqrt{2}g_{1c}g_{2c}/\Delta_2(\Delta_1 + \delta)$ in Ref. [32]. The seemingly noninteracting levels may stay so, or may interact via n photons for $n > 2$ or under external gates.

Effective circuit Hamiltonian: to reduce quantum computation errors all circuit elements should be in the dispersive regime, i.e., with coupling strengths g_{ij} much weaker than frequency detuning $\Delta_{ij} \equiv \omega_i - \omega_j$ [33]. In this limit the Schrieffer-Wolff (SW) transformation [34] simplifies Eq. (1) to this qubit-qubit Hamiltonian:

$$H = \sum_{n_q} \bar{\omega}_q(n_q)|n_q+1\rangle\langle n_q+1| + \sum_{n_1,n_2} \sqrt{(n_1+1)(n_2+1)}$$
$$\times J_{n_1,n_2}(|n_1, n_2+1\rangle\langle n_1+1, n_2| + \text{h.c.}), \quad (2)$$

with dressed frequency $\bar{\omega}_q(n_q)$ being the difference between $\bar{E}_{n_q+1}$ and $\bar{E}_{n_q}$ in dressed basis associated to

interacting Hamiltonian. The qubit-qubit coupling strength within the two photons' limit is

$$J_{n_1 n_2} \equiv g_{12} - \frac{g_{1c}g_{2c}}{2} \sum_{q=1,2} \left[\frac{1}{\Delta_q(n_q)} + \frac{1}{\Sigma_q(n_{qc})} \right], \quad (3)$$

with $\Delta_q(n_q) \equiv \omega_c - \omega_q(n_q)$ and $\Sigma_q(n_q) \equiv \omega_c + \omega_q(n_q)$. One can find the qubit-dressed frequency $\bar{\omega}_q(n_q) = \omega_q(n_q) - g_{qc}^2(n_q + 1)/\Delta_q(n_q)$ and its dressed anharmonicity $\bar{\delta}_q = \delta_q[1 - 2g_{qc}^2/\Delta_q(\Delta_q - \delta_q)]$.

Let us briefly discuss the impact of measurement of qubits. Readout measurement usually takes place by means of weakly coupling a qubit to a resonator with the interaction $H_{qR} = g_{qR}(\hat{a}_q + \hat{a}_q^\dagger)(\hat{a}_R + \hat{a}_R^\dagger)$. The process of eliminating the readout resonator can take place before or after eliminating the coupler. The difference returns some small leftovers in dressed qubit frequency $đ\omega$ and anharmonicity $đ\delta$, which are

$$\frac{đ\tilde{\omega}_2}{g^6} = -\frac{đ\tilde{\omega}_1}{g^6} = \frac{(\Delta + 2\Delta_2)^2(\Delta^2 + \Delta\Delta_2 + \Delta_2^2)}{2\Delta\Delta_2^4(\Delta + \Delta_2)^4}, \quad (4)$$

$$\frac{đ\tilde{\delta}_{1/2}}{2g^6} = -\frac{(\Delta_2 - \delta_{1/2})^3 + (\delta_{1/2} + \Delta_2)\Delta_2^2}{(\Delta_2^3\Delta \mp \delta_{1/2})(\Delta_2 - \delta_{1/2})^4} \pm \frac{2}{\Delta\Delta_2^4}, \quad (5)$$

with universal coupling g and two qubit detuning $\Delta = \omega_2 - \omega_1$, and $\delta_1, \delta_2, \Delta \ll \Delta_2$.

The effective Hamiltonian approach is limited to dispersive regime as shown in Ref. [35], therefore qubits with small frequency detuning must be treated nonperturbatively. Moreover, the external driving Hamiltonian should be treated with methods other than SW such as the method described in Refs. [36,37] to express nonperturbative strong driving impacts.

III. STATIC *ZZ* FREEDOM

The qubit-qubit Hamiltonian (2) has been written for any number of qubit energy levels. Further block diagonalization separates the computational subspace from higher excitations. Within the dispersive regime the computational form of the qubit-qubit Hamiltonian turns out to have the following operator structure:

$$H_{\text{eff}} = \tilde{\omega}_1|10\rangle\langle10| + \tilde{\omega}_2|01\rangle\langle01| + (\tilde{\omega}_1 + \tilde{\omega}_2 + \zeta)|11\rangle\langle11|,$$
$$= -\frac{\tilde{\omega}_1 + \zeta/2}{2}ZI - \frac{\tilde{\omega}_2 + \zeta/2}{2}IZ + \frac{\zeta}{4}ZZ. \quad (6)$$

Defining $E_{n_1 n_2}$ the energy level with qubit 1 and 2 at levels n_1 and n_2, one can find a general definition for the only interaction term present in Eq. (6) based on energy levels:

$$\zeta = E_{11} - E_{10} - E_{01} + E_{00}. \quad (7)$$

This interaction term is called *static ZZ* interaction since it is always present even when qubits are idle. Let us

emphasize that Eq. (7) is an original definition of static ZZ interaction that can be achieved only by taking the operator form of Eq. (6) into account. Perturbation theory can evaluate the following ζ and dressed frequencies within the dispersive regime:

$$\zeta = 2J_{10}^2/(\bar{\Delta} - \bar{\delta}_1) - 2J_{01}^2/(\bar{\Delta} + \bar{\delta}_2), \tag{8}$$

$$\tilde{\omega}_1 = \bar{\omega}_1 - J_{00}^2/\bar{\Delta}, \quad \text{and} \quad \tilde{\omega}_2 = \bar{\omega}_2 + J_{00}^2/\bar{\Delta}, \tag{9}$$

with $\bar{\Delta} \equiv \bar{\omega}_2 - \bar{\omega}_1$. There are a number of divergences in Eq. (8), however since the original definition Eq. (7) is divergence-free, the divergences are the consequence of our perturbative block diagonalization, therefore results in the vicinity of these divergences are inaccurate.

The dressed frequency shifts depend on the coupling strength J_{00}, which causes the $0 \rightarrow 1$ transition in one qubit and the $1 \rightarrow 0$ transition in the other one. As shown in Eq. (9), $J_{00}/\bar{\Delta}$ is subtracted from the frequency of a qubit and the same amount is added to the other one. Therefore, based on the definition Eq. (7), J_{00} does not contribute to the static ZZ coupling strength. However, the contribution of higher excitations is different; J_{01} and J_{10} couple the $0 \leftrightarrow 1$ transition in one qubit and the $2 \leftrightarrow 1$ transition in the other one. The repulsive interaction between E_{11} and the noncomputational levels E_{02} and E_{20} can cancel one another, making ZZ interaction zero, if E_{11} can be in between and near the two noncomputational levels. We find the first few eigenvalues of Hamiltonian (1) in the presence and absence of interaction, and in Fig. 2 show the energy dispersion ($E_{\text{dress}} - E_{\text{bare}}$) of the two sets to clarify how interaction affects energies. Equation (7) still holds valid to the energy dispersion since static ZZ is zero in the absence of interactions, so one can evaluate ζ from Fig. 2. Usually the frequency shifting due to the interaction is much smaller than the energy gap, so this will not change the relative positions of energy levels. In a CSFQ-transmon pair with coupler frequency being far detuned from both qubits within the limit $|\Delta| < |\delta_{1/2}|$, E_{11} falls in between E_{02} and E_{20} making it possible to have repulsion-free E_{11} at a certain detuning frequency. In a transmon-transmon pair with coupler frequency being far detuned from both qubits, E_{11} is in one side of both noncomputational levels E_{02} and E_{20}, which makes the two repulsions sum and not cancel, possibly except at very large detuning frequency, which falls out of the domain of interest for quantum computation.

A pair of idle qubits that interact unwantedly by ZZ interaction accumulate state-dependent phase error. Evolving the idle quantum states $|00\rangle$ and $|11\rangle$ after time t results in the phase $\exp(+i\zeta t/4)$, while the states $|01\rangle$ and $|10\rangle$ return a different phase $\exp(-i\zeta t/4)$. Therefore, all qubits across a circuit accumulate such two-qubit-state-dependent phase error.
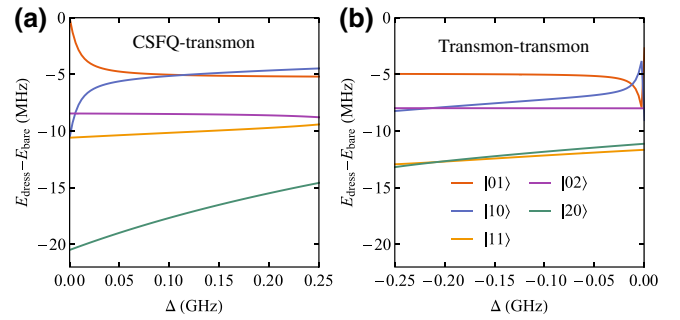

FIG. 2. Difference between interacting and noninteracting energy levels obtained from Hamiltonian (1) in (a) a CSFQ-transmon and (b) a transmon-transmon device. Circuit parameters are similar to those used in Figs. 3(b) and 3(d).

Let us search for the possibility of vanishing phase error for interacting qubits. This can take place by finding ways to eliminate level repulsion between computational and noncomputational levels while computational levels can still interact. Using Eq. (8) one can find the following condition for eliminating ζ:

$$\bar{\Delta} = \frac{\bar{\delta}_1 + \bar{\delta}_2 \gamma^2}{1 - \gamma^2}, \tag{10}$$

with $\gamma \equiv J_{10}/J_{01}$. Ignore counter-rotating terms one can find

$$\gamma = \frac{1 - \delta_1/(2\Delta_2 + \Delta)}{1 - \delta_2/(2\Delta_2 + \Delta)} \frac{1 - \delta_2/\Delta_2}{1 - \delta_1/(\Delta_2 + \Delta)}. \tag{11}$$

The condition of the static ZZ elimination as shown in Eq. (10) makes it possible to investigate such a possibility for certain circuit parameters. Below we consider two types of circuits, a transmon-transmon pair coupled via a coupler, and a CSFQ-transmon pair coupled via a coupler.

CSFQ-transmon pair: a recent experiment has revealed that combining a positive and a negative anharmonic qubit can make ZZ freedom [19]. This freedom can take place in qubits with nonzero J interaction, which allows for entangling them with two-qubit gates. Here we search for circuit characteristics that allow ZZ free qubits. Let us consider $Q2$ being a fixed frequency transmon is coupled to a CSFQ with Δ detuned frequency, i.e., $\omega_1 = \omega_2 - \Delta$. We consider a large Hamiltonian (2) matrix with levels from E_{00} up to E_{04} and E_{40} and block diagonalize to the computational subspace. This determines repulsion between computational and noncomputational levels more accurately. The result has been plotted in Fig. 3(a), showing ZZ coupling strength in colors over a wide domain of CSFQ anharmonicity δ_1 and the frequency detuning Δ. ZZ interaction will have both negative and positive signs with a nontrivial borderline (solid black) between the two regions where the static ZZ coupling is zero. The marked circle indicates the
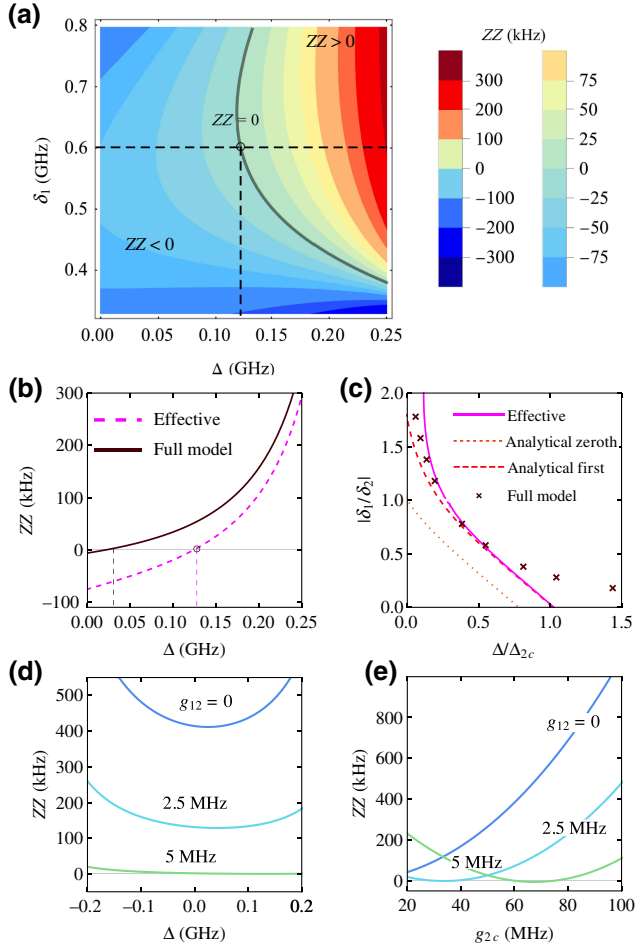
FIG. 3. Static *ZZ* interaction in a CSFQ-transmon device (a)–(c) and in a transmon-transmon device (d) and (e). *Q*1 has the anharmoncity δ_1 and is detuned from a transmon *Q*2 by Δ. (a) Static *ZZ* interaction dependence on CSFQ anharmonicity and qubit-qubit detuning. The two qubits are uncoupled directly, but they are indirectly coupled via a bus resonator with frequency $\omega_c = 6.492$ GHz and coupling strengths $g_{1c} = g_{2c} = 80$ MHz with $\omega_2 = 5.292$ GHz, $\delta_2 = -0.33$ GHz. The effective *ZZ* interaction is positive (negative) in red (blue) areas and it vanishes on the solid lines. (b) Static *ZZ* interaction with $\delta_1 = 0.6$ GHz using the effective (dashed pink) and full model (solid brown) individually. (c) Static *ZZ* freedom criteria via the effective (solid), analytical zeroth-order (dotted), first-order (dashed), and full Hamiltonian model (cross). Static *ZZ* interaction in a transmon-transmon device with $\omega_2 = 4.914$ GHz, $\omega_c = 6.31$ GHz, $\delta_1 = \delta_2 = -0.33$ GHz and direct coupling $g_{12} = 0, 2.5, 5$ MHz as a function of (d) qubit-qubit detuning with $g_1 = 98$ MHz, $g_2 = 83$ MHz, and (e) transmon-resonator coupling strength g_{2c} with $g_{1c} = 98$ MHz and $\Delta = -0.1$ GHz.

parameters of the CSFQ-transmon circuit experimented in Ref. [19] and shows zero static *ZZ* and one can see the marked circle is on the zero *ZZ* borderline.

Figure 3(b) compares two different approaches to determine the static *ZZ* for CSFQ-transmon pair at different detuning frequency: the dashed line obtained from the SW

effective Hamiltonian as found in Eq. (8), the solid line obtains *ZZ* strength from numerical analysis of diagonalizing full Hamiltonian (1). Comparing the two methods reveals that both methods show consistent *ZZ* freedom and that perturbation theory is more accurate in the large Δ domain. Figure 3(c) shows the parameters at which the static *ZZ* is zero. The parameters used here are the normalized frequency detuning Δ by transmon-coupler detuning Δ_2 and the magnitude of anharmonicity ratio. Crossed points show exact results from diagonalizing of the full Hamiltonian, and the solid line is obtained from Eq. (10). The two dashed lines are analytical solutions of Eq. (10) in the zeroth and first order in $|\delta_2/\Delta_2|$. For obtaining these analytical solutions we define the qubits anharmonicities by $\delta_1 = k\delta$, $\delta_2 = -\delta$ with $k, \delta > 0$. We consider no direct coupling between qubits and the universal qubit-coupler coupling strength g, and $\Delta = b\Delta_2$. Substituting these parameters in Eq. (11) evaluates $J_{10}/J_{01} = (1 + a)(1 + b)(ak - b - 2)/(2 + b + a)(ak - b - 1)$, with $a \equiv \delta/\Delta_2$. Equation (10) can be simplified in the absence of a to $k = (2 + b - 3b^2 - 2b^3)/(2 + 5b + b^2)$, i.e., zeroth-order solution. Adding the first order of a increases the solution precision. One can see for CSFQ anharmonicity being greater than transmon anharmonicity the analytical approximation is trustable.

Transmon-transmon pair: in such a pair both anharmonicities are negative. Based on the perturbation theory, let us first make some estimation about the possibility of *ZZ* freedom. A trivial possibility is when $J_{01} \approx J_{10} \approx 0$, more precisely direct coupling g_{12} cancels out the indirect couplings in Eq. (3). This freedom has been realized recently in several experiments [24–26,38]. However, non-interacting qubits cannot be entangled at such an operating point and are not useful for quantum computation. Searching for *ZZ* freedom in the presence of *J* coupling, results in such a possibility with qubit-coupler coupling g_{qc} being equal or larger than the qubit-resonator frequency detuning Δ_q, which goes beyond the dispersive regime and perturbatively invalid. Exact numerical result with the full Hamiltonian does not show any possibility for *ZZ* freedom in transmon-transmon pairs within the quantum computational domain of parameters. Other approaches, e.g., two transmons coupled via a tunable coupler in principle can achieve *ZZ* freedom [39,40], but in reality it always varies such an interaction above zero [41–43].

Although *ZZ* freedom cannot be achieved for an interacting pair of transmons, one can, however, achieve its suppression by tuning circuit parameters. For this purpose, let us consider two transmons with almost the same anharmonicity and different frequencies. We numerically simulate the circuit and extract static *ZZ* by numerical diagonalization of the full Hamiltonian model. Figure 3(d) shows static *ZZ* coupling strength decreases by lowering the magnitude of detuning frequency Δ. This has been studied for three direct couplings g_{12}. At $g_{12} = 5$ MHz

the qubits are J-interaction-free. Interestingly, the weaker g_{12} cases show that suppression of ZZ interaction can be achieved within a rather large domain of detuning frequency Δ, making it possible to design a transmon-transmon circuit with suppressed ZZ interaction within the dispersive regime $\Delta \gg J$. Figure 3(e) shows how ZZ coupling changes by tuning transmon-resonator coupling g_{2c}. Although the zero ZZ points belong to J-interaction-free transmons, in their vicinity, however, one can see a large class of transmons that not only interact but also their unwanted ZZ interaction is suppressed.

IV. TWO-QUBIT GATE: CROSS RESONANCE

Let us consider a two-qubit gate that rotates a qubit depending on the state of another qubit. Here we consider the CR gate—a microwave pulse with the oscillation frequency equal to the frequency of $Q2$, which is applied on $Q1$. For this gate $Q2$ is target and $Q1$ is control qubit. The CR driving Hamiltonian is,

$$H_{CR} = \Omega \cos(\omega_d t) \sum_{n_1} (|n_1\rangle\langle n_1 + 1| + \text{h.c.}), \quad (12)$$

with Ω being the amplitude and $\omega_d = \tilde{\omega}_2 + \zeta/2$ being the frequency of driving. We let Eq. (12) corotate with the free Hamiltonian Eq. (2) by transforming it by $R = \sum_n \exp(-i\omega_d t \hat{n})|n\rangle\langle n|$, $H_{CR} \rightarrow R^\dagger(H_{CR})R - iR^\dagger R$. Rotating-wave approximation (RWA) helps to simplify fast oscillating terms making the Hamiltonian time independent.

Driving qubits externally by weak amplitude pulses will not harm the perturbative block-diagonalization scheme $\Omega \ll \Delta, g$. Since this domain of amplitude is too narrow we also compare perturbative transformation with nonperturbative least action transformation. We need a unitary transformation T that can be constructed under a very weak constraint motivated by the idea that the only action that the transformation should perform is to bring H into block-diagonal form and does nothing otherwise [37]. Such a block-diagonalization technique has been previously worked out in chemistry in Ref. [36], namely the "least action" (LA) block diagonalization. This transformation can be constructed after determining the eigenvectors of the Hamiltonian H. The matrix of all eigenvectors S, and a block-diagonal part of it S_{BD}, help to construct the transformation matrix T in the following way:

$$T = SS_{BD}^\dagger \left(S_{BD}S_{BD}^\dagger \right)^{-1/2}. \quad (13)$$

Block diagonalizing the CR-driven multilevel interacting qubits by transforming their Hamiltonian into $T(H +$

$H_{CR})T^\dagger$ leaves us with the following qubit-qubit Hamiltonian in the computational subspace:

$$H = \alpha_{ZI}\frac{ZI}{2} + \alpha_{IX}\frac{IX}{2} + \alpha_{ZX}\frac{ZX}{2} + \alpha_{ZZ}\frac{ZZ}{4}$$
$$+ \alpha_{ZY}\frac{ZY}{2} + \alpha_{IY}\frac{IY}{2}. \quad (14)$$

Although the same operator structure as Eq. (14) can be found by perturbative block diagonalization, deviations from perturbation, however, are visible within the strong driving domain. We keep a record of both sets of coupling strengths and compare them in the results taken in the rest of the paper. Among all terms that appear in Eq. (14), the only desired interaction is ZX as combining it with single-qubit rotations provides two-qubit CNOT gate. Classical crosstalk effect, whose nature is still the subject of research, can add up additional terms in the Hamiltonian Eq. (14) by changing the coupling constant of IX and IY terms. The ZY term can be eliminated by calibrating the global phase of CR pulse and this leaves us with its sibling ZX interaction. Moreover, applying an active cancellation pulse on target qubit with fine-tuned amplitude and phase can eliminate IY and IX terms [44]. All these help to obtain gate ZX along with unwanted ZZ term. Numerical results in a CSFQ-transmon circuit is plotted in Fig. 4. As one can see in weak amplitudes, perturbation and nonperturbative results overlap, however, as expected, they grow differently by increasing the driving amplitude.

The ZZ interaction in a CR-driven qubit-qubit circuit has two parts: (1) the static part due to computational level repulsion induced by noncomputational levels, and (2) a dynamical ZZ part induced by CR gate manipulation on the level repulsion. It is worthwhile to emphasize that since the CR gate produces interactions other than ZZ coupling in Hamiltonian (14), such as ZX, in the presence of the CR gate the ZZ coupling cannot be identified from Eq. (7) any more.
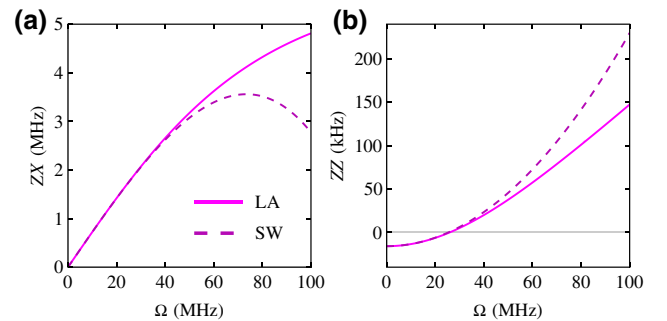

FIG. 4. ZZ and ZX coupling strengths in a CSFQ-transmon pair versus CR amplitude Ω, using Schrieffer-Wolff transformation (dashed) and least action transformation (solid). $\Delta = 0.1$ GHz and the other parameters are similar to Fig. 3(b).
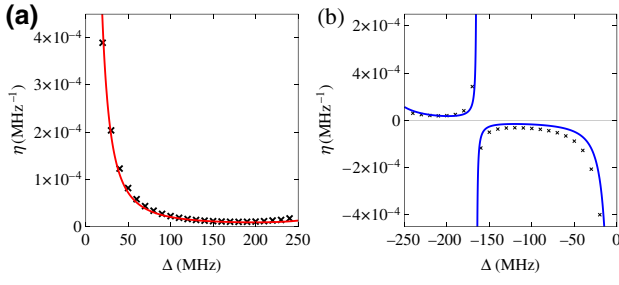
FIG. 5. η as a function of qubit frequency detuning, (a) CSFQ-transmon devices similar to Fig. 3(b), and (b) transmon-transmon devices similar to Fig. 3(d) with $g_{12} = 2.5$ MHz. Cross points are numerical results from LA transformation and the solid line from SW transformation.

Perturbation theory obtains that in the weak driving limit the dynamic *ZZ* component depends quadratically on CR amplitude Ω [37]. Therefore, the general structure of *ZZ* strength is

$$\alpha_{ZZ} = \zeta + \eta\Omega^2 + O(\Omega^3), \qquad (15)$$

with η depending on qubit parameters such as anharmonicity and detuning frequency, as well as coupling strengths. Using SW perturbation theory one can analytically determine it in the weak driving limit, see Appendix D.

The nonperturbative block diagonalization of LA transformation reproduces weak coupling results, however adds higher-order corrections denoted by $O(\Omega^3)$ that contribute to deviations from perturbation theory in the strong driving limit. In Fig. 5 we plot perturbative η in solid lines and the LA nonperturbative η in cross points, in (a) for a CSFQ-transmon and in (b) for a transmon-transmon circuit. One can see that CSFQ-transmon pair carries positive η, which makes the CR gate add up the positive dynamic *ZZ* component on top of the static part. This may result in suppression of total *ZZ* strength if the static part is negative. In the transmon-transmon circuit η is negative only at small detuning frequency. Perturbation theory shows divergence, however LA transformation finds that the divergence is unphysical and that *ZZ* strength remains finite.

V. DYNAMICAL *ZZ* CANCELLATION

In the previous section we study the impact of CR gate on level repulsion that results in variation of total *ZZ* interaction from its value at idle qubits. Here we determine *ZX* and *ZZ* strengths for some CSFQ-transmon and transmon-trasnmon pairs at a large domain of CR pulse amplitudes. We show in examples how the dynamic *ZZ* interaction may or may not cancel the static one. This provides a unique opportunity to tune circuit parameters for obtaining opposite sign static and dynamic *ZZ* components. CR amplitude can control the magnitude of the dynamic part and allows

for vanishing total *ZZ* strength. In this section we show the dynamic *ZZ* freedom can take place in transmon-transmon as well as CSFQ-transmon pairs. Moreover, the freedom is persistent as long as CR gate is active and this simultaneously improves the CR gate fidelity.

In Fig. 6 we study two types of qubit-qubit setups: five CSFQ-transmon samples labeled from 1 to 5, and five transmon-transmon samples labeled from 6 to 10. The corresponding energy levels are depicted in Fig. 6(a). In the diagram, the energy level of $|010\rangle$, $|100\rangle$, and $|001\rangle$ show their differences in the coupler and the two qubit frequencies. The noncomputational states $|002\rangle$ and $|200\rangle$ in transmon-transmon circuits are both below $|101\rangle$ and in CSFQ-transmon circuits on its two sides. Since in these examples the coupler frequency is far detuned from qubits, the repulsions between $|101\rangle$ and noncomputational levels in transmon-transmon devices have the same sign and sum, and in CSFQ-transmon devices have different signs and subtract.

Applying CR pulse produces the desired *ZX* entanglement between the two qubits. We determine interaction strength from nonperturbative LA transformation. In Figs. 6(b) and 6(c) the *ZX* strengths of CSFQ-transmon and transmon-transmon devices are plotted, respectively. The strength of *ZX* coupling increases with the CR amplitude, however its growth starts to diminish as soon as E_{11} comes near to other levels. Figures 6(d) and 6(e) show total *ZZ* strength for CSFQ-transmon and transmon-trasmon devices. In samples 1–3 the static *ZZ*, i.e., at $\Omega = 0$, are negative and in 4 and 5 positive. The static *ZZ* remains the same at all driving amplitudes Ω, i.e., as it is always on, however, adding the positive dynamic *ZZ* component the total suppresses in 1–3 and can go zero at certain amplitude, however in 4 and 5 the cancellation cannot take place. Interestingly, similar *ZZ* freedom takes place in transmon-transmon circuits as it can be seen in devices 8–10. Notice that device 6 is the IBM experimental device used in Ref. [44] and we can see it does not show total *ZZ* freedom.

Determining the CR amplitude at which total *ZZ* freedom may take place requires measuring the static *ZZ* coupling. This can take place by performing a Ramsey pulse sequence on Q1 at state $|0\rangle$ and repeating it at state $|1\rangle$. The difference in frequency between these experiments determines the static *ZZ* rate [19]. Once the static *ZZ* is determined, one can use Eq. (15) to determine how much of the CR amplitude is required to set the total *ZZ* to zero. Equivalently one can also perform a quantum Hamiltonian tomography after applying the CR pulse, by measuring the target qubit state after projecting it on *X*, *Y*, and *Z* axis of the Bloch sphere [44]. This determines the Pauli coefficients of Eq. (14), including *ZZ* term.

We can use SW perturbation theory to determine the interaction strengths analytically and we expect sufficient accuracy of the results in the weak driving limit. By solving the equation $\alpha_{ZZ} = 0$, the condition for dynamical
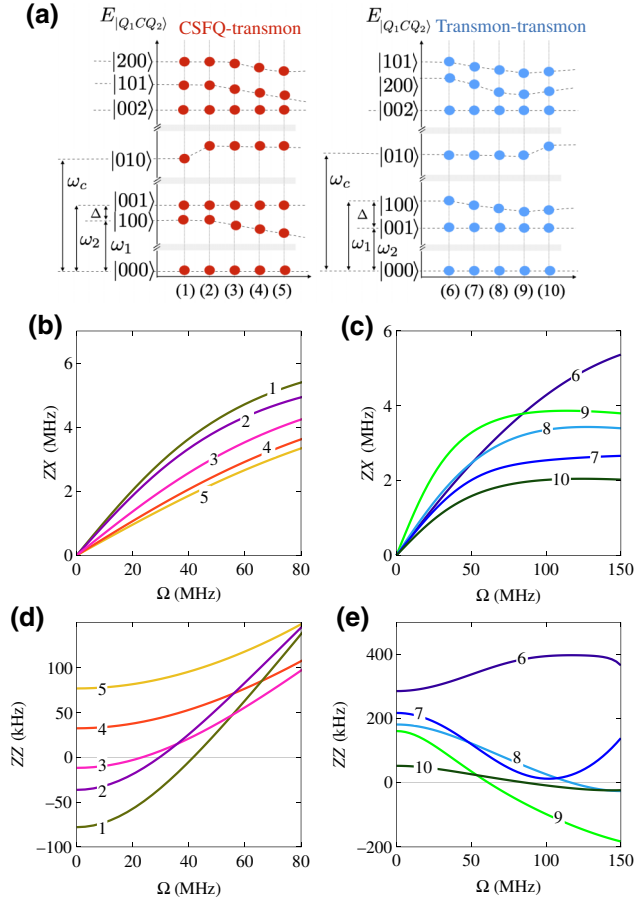
FIG. 6. (a) Energy diagrams for five CSFQ-transmon circuits (1–5) and five transmon-transmon circuits (6–10). The coupling strength under CR gate using nonperturbative least action transformation for (b) ZX interaction in devices 1–5, (c) ZX interaction in 6–10, (d) ZZ interaction in 1–5, and (e) ZZ interaction in 6–10. Common parameters in 1–5 are $\delta_{1/2} = 0.6,\ -0.33$ GHz, $g_{1c/2c} = 80$ MHz, and $g_{12} = 0$. In 1, $\Delta = 70$ MHz and $\Delta_2 = 1.1$ GHz. In 2–5, $\Delta = 70,\ 105,\ 150,\ 180$ MHz and $\Delta_2 = 1.2$ GHz. Common parameters in 6–10 are $\delta_{1/2} = -0.33$ GHz, $g_{1c/2c} = 98,\ 83$ MHz, and $g_{12} = 2.5$ MHz. In 6–9, $\Delta = -200,\ -150,\ -100,\ -50$ MHz and $\Delta_2 = 1.4$ GHz. In 10, $\Delta = -70$ MHz and $\Delta_2 = 2$ GHz.

ZZ freedom in the first order of Δ/δ_2 can be obtained at the particular CR amplitude (in the limit of $\Delta/\delta_2 \ll 1$):

$$\Omega^* = |\Delta|\sqrt{\frac{2(r + \gamma^2)}{r + \gamma(2 + \gamma)}}\sqrt{1 - C\frac{\Delta}{\delta_2}}, \qquad (16)$$

with $C \equiv [1/2 + 2\gamma + \gamma^2 + r^2 + r\gamma(2 + \gamma) + \gamma^2(1 + 2\gamma^2)/2r]/\{(r + \gamma^2)[r + \gamma(2 + \gamma)]\}$ and $r \equiv \delta_1/\delta_2$. Table I compares the CR amplitude Ω^* at which dynamical ZZ cancels out the static ZZ interaction. The amplitude Ω^* is determined using three different methods for devices 1–10. In the row labeled by LA we use the nonperturbative least action method to determine total ZZ and find
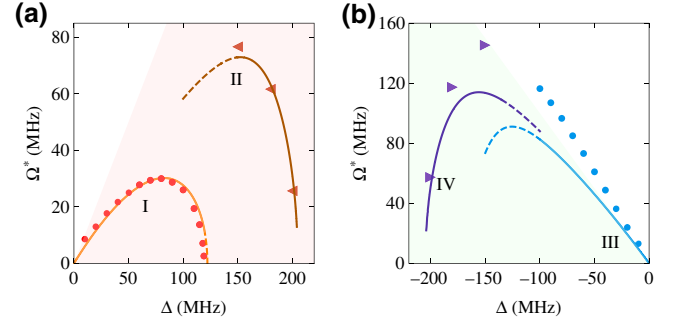

FIG. 7. The amplitude of dynamical ZZ freedom versus qubit detuning frequency, (a) for CSFQ-transmon pairs with parameters similar to circuit 2–5 devices, I with $\delta_{1/2} = 0.6,\ -0.33$ GHz and II with $\delta_{1/2} = 0.41,\ -0.39$ GHz, (b) for transmon-transmon pairs with parameters similar to 6–9 devices, III with $\delta_{1/2} = -0.33,\ -0.33$ GHz and IV with $\delta_{1/2} = -0.41,\ -0.33$ GHz. Lines are perturbative results, dots and triangles are results taken from nonperurbative least action. Shaded area shows the validity domain of perturbation theory.

where it is zero. In the $O(n)$ row we use the SW-evaluated static ZZ coupling ζ of Eq. (8) and the SW-evaluated η in Appendix D and substitute them in Eq. (15) to obtain at what amplitude ZZ becomes zero. Below it we present the results from Eq. (16) and in the last row we evaluate the ratio of Δ/δ_2 in each device. One can see the results are better consistent in the limit of $\Delta/\delta_2 \ll 1$.

Let us further study the CR amplitudes at which dynamic freedom takes place. In what comes next we work with the parameters of the devices 2–5 CSFQ-transmons and the devices 6–9 transmon-transmons, except that we keep detuning frequency Δ a variable and change the anharmonicity at large detuning. We work out the CR amplitude at which dynamic ZZ freedom can take place within a large range of Δ in Figs. 7(a) and 7(b). Dots and triangles show results taken using nonperturbative least action transformation and lines are SW perturbative results. Shaded area shows the validity domain of perturbation theory in the parameter Ω/Δ, these results show that dynamical cancellation is not limited by the qubit-qubit detuning. One can see perturbation theory is a crude approximation for transmon-transmon devices, while it works better for CSFQ-transmon pairs. This is mainly because the static ZZ strength in transmon-transmon pairs is usually large and then cancelling it requires strong driving amplitudes whose accuracy falls outside of perturbation techniques.

One of the noticeable characteristics of dynamic ZZ freedom in CSFQ-transmon pairs as seen in Fig. 7(a) is that by increasing detuning frequency first cancellation amplitude increases, and at larger detuning frequency the amplitude squeezes. In transmon-transmon pairs of Fig. 7(b) the amplitude almost monotonically changes. These behaviors

TABLE I. Ω^* from different methods in devices 1–10 in MHz. "No" indicates devices with no dynamic *ZZ* freedom.

	(1)	(2)	(3)	(4)	(5)	(6)	(7)	(8)	(9)	(10)
LA	42	30	24	No	No	No	No	115	61	82
$O(n)$	41	31	24	No	No	No	71	83	46	62
Eq. (16)	41	34	40	20	No	110	104	81	46	61
Δ/δ_2	0.11	0.11	0.17	0.25	0.3	0.61	0.45	0.3	0.15	0.21

are consistent with what we find above for the way how ζ and η scale with detuning Δ.

VI. CR GATE ERROR

A pair idle qubits carry a Hamiltonian that contains *ZI*, *IZ*, and *ZZ* Pauli coefficient. CR gate changes some of these coefficients and also as shown in Eq. (14) introduces some unwanted interactions. Instead of a single CR pulse one can use an echoed CR pulse on the control qubit, which consists of a CR pulse for duration *t*, a π rotation about the *X* axis, a π-shifted CR pulse for the same duration, and another π rotation about the *X* axis. Applying an echoed CR gate on the control qubit along with an active cancellation pulse with fine-tuned phase and amplitude on the target qubit eliminate all unwanted interactions and leave us with the following couplings only: *ZX* and *ZZ*. For details see Refs. [45,46]. Applying the echoed CR gate results in an oscillation in the target qubit with the frequency $f_{\text{ECR}} = 2\sqrt{\alpha_{ZX}^2 + \alpha_{ZZ}^2/4} \approx 2\alpha_{ZX}$.

To quantify the performance of echoed-CR gate on dynamic *ZZ* free qubits, we numerically simulate the CR gate for several devices in Fig. 6. Here we consider the gate length that includes two rounded square CR pulses with ignorable rise and fall times, and each of which is followed by a 40-ns-long π pulse. As described in Ref. [19], the two-qubit gate will be of the form $\exp[-i\theta ZX/2]$ with $\theta = 2\pi f_{\text{ECR}}\tau$ and τ being the flat-top length of each CR tone. Setting $\theta = \pi/2$ makes a unitary gate that entangles the two qubits. When performing a CR gate, the flap top of the single CR tone τ satisfies $\tau = 1/8\alpha_{ZX}$ when CR driving amplitude is small, and the total gate length $t_g = (2\tau + 80)$ ns.

We simulate an echoed CR pulse sequence for implementing a $ZX(\pi/2)$ gate. We compute the two-qubit error per gate by evaluating how the unitary evolution of the echoed CR gate evolves an initial state. The presence of *ZZ* interaction determines a state-dependent phase error in the desired state. We evaluate the infidelity of final state. Figure 8 shows the CR gate error caused by *ZZ* interaction as a function of gate length and qubit-qubit detuning with infinite coherence time. In these plots we ignore the decoherence effect on the gate as we assume that qubits can have desirably long coherence times T_1 and T_2. In CSFQ-transmon devices 2 and 3 where total *ZZ* can be dynamically set to zero, we can get the *ZX* rotation free

of parasitic *ZZ* interaction and therefore the gate error drops at certain gate times. For device 2, Figs. 6(a) and 6(d) show that where the dynamic freedom takes place is at $\alpha_{ZX} \sim 2.7$ MHz. Such a frequency requires $\tau \sim 46$ ns for each CR pulse to perform $\pi/2$ *ZX* rotation. Considering the second CR pulse and the additional π rotation will sum the total echoed-CR pulse length to 172 ns. In Fig. 8(a), one can see that device 2 performs a perfect gate with no error at this gate length. In device 3, the cancellation takes place at a α_{ZX} that is smaller by a factor of 1/1.7 and this causes the prolongation of the gate to become 235 ns. While the gate error in devices 4 and 5 decreases as the gate becomes longer due to reduction of total *ZZ* interaction, the gate error in the absence of decoherence can, however, be in the scale of 10^{-3}.

In transmon-transmon devices almost similar behavior is expected and one can find errorless $ZX(\pi/2)$ in dynamical *ZZ* free trasmons. The perfect gate times in devices 8 and 9 are shorter compared to CSFQ-transmon pairs. The reason for such an improvement is that in these transmon-transmon devices the dynamic cancellation takes place at an amplitude that causes faster *ZX* rotation. However, one can see in Fig. 8(b) that some transmon-transmon devices such as 7, 8, and 9 show some cutoff in their minimum gate length for $ZX(\pi/2)$ rotation. Figure 6(c) shows that the α_{ZX} rate starts to saturate after some amplitudes and cannot increase any more. This saturation puts limitation on flap-top length τ such that it cannot become shorter than a minimum, i.e., $\tau_{\min} = 1/8\alpha_{ZX}^{\max}$. This will introduce a cutoff on echo-CR gate length to become limited to longer than $t_g^{\min} = (1/4\alpha_{ZX}^{\max} + 80)$ ns. For instance, device 7 in Fig. 6(c) reaches a saturation around 2.5 MHz and this introduces a gate time cutoff below 180 ns as shown in Fig. 8(b). Moreover, device 7 shows some dynamic *ZZ* suppression to a minimum of approximately 20 kHz and our analysis shows that at this gate time the error although cannot be eliminated but it can be suppressed to 10^{-5} for transmons without decoherence error.

Overall, to perform an ideal cross-resonance gate, the following two conditions should be satisfied: (1) static *ZZ* interaction is zero when two qubits are in the idle state; (2) maximum *ZX* component and zero total *ZZ* interaction should be realized synchronously when the two qubits are under driving. Although it is more convenient to implement dynamical *ZZ* cancellation on a CR gate, this approach can still be generalized to suppress the built-in
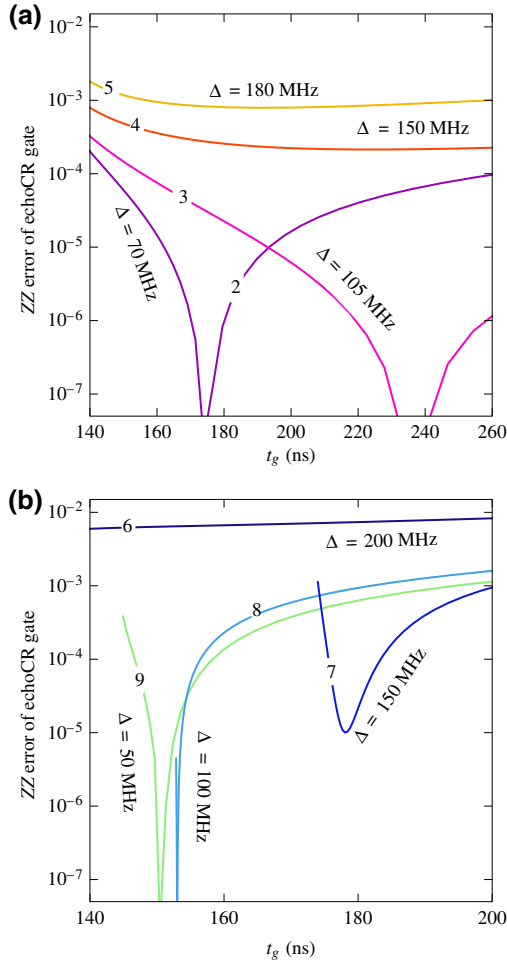
FIG. 8. *ZZ* error of the echo CR gate as a function of gate length and two-qubit detuning in (a) CSFQ-transmon devices and (b) transmon-transmon devices.

ZZ interaction in any gates. In large quantum processors we expect to have a huge number of pairs of qubits that have nonzero *ZZ* interaction contributing to the gate error, if we apply the well-designed CR-type pulses on a pair of qubits and make a 2π rotation by *ZX* operator, leaving qubits with no *ZX* rotation. Such a system will not suffer from parasitic *ZZ* interaction at all while it maintains its original state.

VII. DISCUSSION

In this paper, we study the parasite *ZZ* interaction and the possibility of freeing qubits from it. Zeroing the *ZZ* strength can take place in two ways: (1) in idle qubits, circuit parameters can be found such that the static *ZZ* strength becomes zero. The static *ZZ* freedom can take place in qubits with opposite sign anharmonicity; (2) in driven qubits with a microwave pulse, an additional *ZZ* component adds on top of the static part making it possible to cancel it out, making total *ZZ* strength zero. This

dynamic *ZZ* freedom takes place at a driving amplitude that could be determined from circuit QED.

Eliminating the static *ZZ* will make idle qubits no longer suffer from accumulating state-dependent phase error across the circuit. Moreover, when a two-qubit gate is active, eliminating all of the parasitic *ZZ* interaction as long as the gate is active, results in a large increase in the gate fidelity.

Our derivation is restricted to two interacting qubits. The *ZZ* free qubits can have many advantages; for instance, a complete understanding of pairwise suppression of *ZZ* interaction in a large circuit with many qubits can result in quantum computation on the circuit with less error. Future research is needed to study clusters of interacting three-body and higher many-body qubits. Although the general expectation is that the coupling strength of these terms to be weaker than pairwise interactions, however, they can generate additional gate error as well as crosstalk error across the circuit. Elimination of parasitic many-body interactions such as *ZZZ* couplings depends on qubit connectivity, i.e., whether qubits are connected in a loop or are in linear connection. This paves the way toward optimal operation for reducing quantum computational error to below the threshold of error correction.

APPENDIX A: CSFQ HAMILTONIAN

Figure 1(a) helps to write the CSFQ Lagrangian $\mathcal{L} = \frac{1}{2}(\Phi_0/2\pi)^2\{(C_{sh} + \alpha C_J)(\dot{\phi}_1 - \dot{\phi}_3)^2 + C_J(\dot{\phi}_1 - \dot{\phi}_2)^2 + C_J(\dot{\phi}_2 - \dot{\phi}_3)^2\} + E_J\{\cos(\phi_1 - \phi_2) + \cos(\phi_2 - \phi_3) + \alpha \cos(2\pi f - \phi_1 + \phi_3)\}$ with external flux number $f \equiv \Phi_{ext}/\Phi_0$ and the external magnetic flux Φ_{ext} penetrating the loop. Defining phase variables $\phi = \phi_1 - \phi_3$ and $\phi' = \phi_1 - 2\phi_2 + \phi_3$ can help to uncouple degrees of freedom. Considering the charging energy of a typical capacitance C being $E_C \equiv e^2/2C$, the effective capacitance associated with the modes ϕ and ϕ' are $C \equiv C_{sh} + \alpha C_J + C_J/2$ and $C' = C_J/2$, respectively. The key to C-shunt flux qubit is the large shunting capacitance $C_{sh} \gg C_J$, which indicates that the mode ϕ' oscillates with an order of magnitude larger frequency compared to the oscillation of ϕ mode. Therefore, the large charging energy of ϕ' mode makes its contribution to qubit potential negligible. This makes qubit potential separable and eventually the ϕ' mode can be safely discarded from dynamics. This helps to write down the CSFQ qubit Hamiltonian $H = 4E_C n^2 - 2E_J \cos(\phi/2) - \alpha E_J \cos(2\pi f - \phi)$. The one-dimensional potential has a single minimum for $\alpha < 1/2$, which is the

domain of our interest, otherwise indicates double minima. Bringing the qubit to the bottom of its potential minimum, namely the SS, will produce the longest T_2 coherence for the qubit.

In comparison to a transmon, higher-order terms (> 4) in the expansion of the CSFQ potential also contribute to the eigenvalues, which will change the zero-point fluctuation to an unknown number. To be more precise, the Hamiltonian can be quantized in terms of field operators, e.g., $n = i(\hat{a} - \hat{a}^\dagger)/2\xi$ and $\phi = \xi(\hat{a} + \hat{a}^\dagger)$ with ξ being the expansion parameter, which will minimize the total energy, the normal-ordered Hamiltonian then can be written as

$$
\begin{aligned}
H = {} & -\frac{E_c}{\xi^2}(\hat{a}^\dagger - \hat{a})^2 + \sum_{u=0}^{\infty} \xi^{2u+2} \sum_{v=0}^{u} \frac{U_{2u+2}(\phi_0)}{2^{u-v}(u-v)!} \\
& \times \sum_{w=-(v+1)}^{v+1} \frac{(\hat{a}^\dagger)^{v+1+w}(\hat{a})^{v+1-w}}{(v+1+w)!(v+1-w)!} \\
& + \sum_{u=0}^{\infty} \xi^{2u+1} \sum_{v=0}^{u} \frac{U_{2u+1}(\phi_0)}{2^{u-v}(u-v)!} \\
& \times \sum_{w=-(v+1)}^{v} \frac{(\hat{a}^\dagger)^{v+1+w}(\hat{a})^{v-w}}{(v+1+w)!(v-w)!},
\end{aligned}
\tag{A1}
$$

with $U_n(\phi_0) \equiv \partial^n U(\phi_0)/\partial\phi_0^n$ and $U(\phi_0) \equiv -2E_J \cos\phi_0/2 - \alpha E_J \cos(2\pi f - \phi_0)$ and ϕ_0 being the phase of minimum $U(\phi_0)$, i.e., $\phi_0 = -2\pi\alpha(\delta f)/(1/2 - \alpha)$, which vanishes at the sweet spot. By solving the Schrödinger equation, the eigenenergies E_n can be obtained using perturbation theory. Unperturbed eigenvalues $E_n^{(0)}$ and the first three-order corrections are given by

$$
\begin{aligned}
E_n^{(0)} = {} & \left(\sum_{l=1}^{L} \frac{U^{(2l)}\xi^{2l}}{(2l-2)!!} + \frac{2E_C}{\xi^2} \right) n \\
& + \sum_{k=2}^{L} \sum_{l=2}^{L} \frac{U^{(2l)}\xi^{2l}}{(2l-2k)!!} \frac{n!}{(n-k)!}, \\
E_n^{(1)} = {} & 0, \\
E_n^{(2)} = {} & \sum_{k \neq n}^{n+L} \frac{V_{nk}^2}{E_n^{(0)} - E_k^{(0)}}, \\
E_n^{(3)} = {} & \sum_{k \neq n}^{n+L} \sum_{m \neq n}^{n+L} \frac{V_{nm}V_{mk}V_{kn}}{(E_n^{(0)} - E_k^{(0)} t)(E_n^{(0)} - E_m^{(0)})},
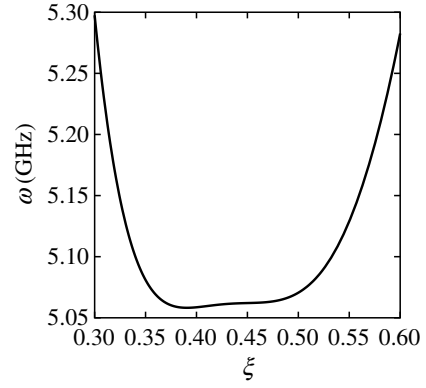\end{aligned}
\tag{A2}
$$

FIG. 9. Frequency as a function of ξ at the sweet spot. Simulation parameters $E_C = 0.292$ GHz, $E_J = 108.9$ GHz, $\alpha = 0.43$, and $f = 0.5$.

with

$$
\begin{aligned}
V_{nm} = {} & x_{|m-n|,|m-n|}\sqrt{\frac{\max(m,n)!}{\min(m,n)!}} \\
& + \sum_{s=0}^{\min(m,n)} x_{\max(m,n)-s,\min(m,n)-s}\sqrt{\frac{n!m!}{s!}} \\
x_{a,b} = {} & \delta_{ab} \sum_{k=a}^{L} \sum_{u=0} \Theta(k-a-2u) \frac{U^{(k)}\xi^k}{(k-a)!!a!} \\
& + (1-\delta_{ab}) \sum_{k=a}^{L} \sum_{u=0} \Theta(k-a-2u) \frac{U^{(k+b)}\xi^{k+b}}{b(k-a)!!a!} \\
& - \delta_{a2}\delta_{b2}\frac{E_C}{\xi^2}.
\end{aligned}
$$

Sum up unperturbed energy and all three-order corrections, one can obtain the analytical formula of CSFQ eigenvalues, then frequency $\omega_{01} = (E_1 - E_0)/\hbar$ and anharmonicity $\delta = (E_2 - 2E_1 + E_0)/\hbar$ can be evaluated. Here is an example to illustrate how to find these parameters. Consider a CSFQ with $E_C = 0.292$ GHz, $E_J = 108.9$ GHz, $\alpha = 0.43$, and $f = 0.5$. Firstly, expand the potential to 20th order ($L = 10$) at the sweet spot and plot the frequency f_{01} as a function of ξ. Determine ξ by finding the minimum as shown in Fig. 9 (approximately $\xi \approx \phi_{ZPF}/\sqrt{2}$), then substitute ξ back to Eq. (A2), the corresponding frequency and anharmonicity spectra are shown in Fig. 10.

APPENDIX B: FULL HAMILTONIAN

To understand how the interaction terms change the bare basis, we apply the full Hamiltonian (1) on the states $|n_1, n_c, n_2\rangle$. Consider the first order of g_{ij} ($i \neq j$ and $i,j =$
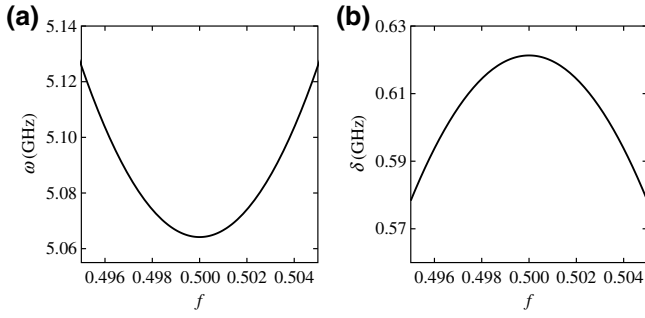
(a)

(b)

FIG. 10. Frequency (a) and anharmonicity (b) as a function of external flux f using perturbation theory.

$1, 2, c$), the result is written as

$$
\begin{aligned}
\hat{H}|n_1, n_c, n_2\rangle \\
= [\omega_1(n_1) + \omega_c(n_c) + \omega_2(n_2)]\,|n_1, n_c, n_2\rangle \\
+ g_{12}[\sqrt{n_1 n_2}\,|n_1 - 1, n_c, n_2 - 1\rangle \\
+ \sqrt{n_1(n_2 + 1)}\,|n_1 - 1, n_c, n_2 + 1\rangle \\
+ \sqrt{(n_1 + 1)n_2}\,|n_1 + 1, n_c, n_2 - 1\rangle \\
+ \sqrt{(n_1 + 1)(n_2 + 1)}\,|n_1 + 1, n_c, n_2 + 1\rangle] \\
+ g_{1c}[\sqrt{n_1 n_c}\,|n_1 - 1, n_c - 1, n_2\rangle \\
+ \sqrt{n_1(n_c + 1)}\,|n_1 - 1, n_c + 1, n_2\rangle \\
+ \sqrt{(n_1 + 1)n_c}\,|n_1 + 1, n_c - 1, n_2\rangle \\
+ \sqrt{(n_1 + 1)(n_c + 1)}\,|n_1 + 1, n_c + 1, n_2\rangle] \\
+ g_{2c}[\sqrt{n_2 n_c}\,|n_1, n_c - 1, n_2 - 1\rangle \\
+ \sqrt{n_2(n_c + 1)}\,|n_1, n_c + 1, n_2 - 1\rangle \\
+ \sqrt{(n_2 + 1)n_c}\,|n_1, n_c - 1, n_2 + 1\rangle \\
+ \sqrt{(n_2 + 1)(n_c + 1)}\,|n_1, n_c + 1, n_2 + 1\rangle]
\end{aligned}
$$

The equation above shows that when interactions turn off, $|n_1, n_c, n_2\rangle$ is the eigenstate of the noninteracting Hamiltonian, when we turn on the interactions, level crossing takes place with the coupling strength scaling with the first order of g_{ij} as shown in Fig. 1(c).

APPENDIX C: PRINCIPLE OF LEAST ACTION

Consider a general $d \times d$ Hermitian Hamiltonian H, which can be transformed into a block-diagonal matrix $\mathscr{H}$ using Eq. (13) with two blocks $\mathscr{H}_{nn}$ and $\mathscr{H}_{mm}$, where n and m are the dimensions of the blocks and satisfy $d = n + m$ and $n \leq m$. The corresponding matrix of all eigenvectors S can also be divided into four blocks, namely

$$
S = \begin{pmatrix} S_{nn} & S_{nm} \\ S_{mn} & S_{mm} \end{pmatrix}. \tag{C1}
$$

As described in Ref. [36], the unitary transformation T can be simplified as $T = U(U^\dagger U)^{-1/2}$ where

$$
U = \begin{pmatrix} 1 & X \\ -X^\dagger & 1 \end{pmatrix}, \quad U^\dagger U = \begin{pmatrix} 1 + XX^\dagger & 0 \\ 0 & 1 + X^\dagger X \end{pmatrix}, \tag{C2}
$$

with $X = -(S_{mn}S_{nn}^{-1})^\dagger = S_{nm}S_{mm}^{-1}$. Therefore, only part of the eigenvector matrix S is needed, for example, the first n eigenvectors. To obtain the blocks in the computational subspace in a large matrix, we first decouple the computational subspace from higher levels using the principle of least action above, and then repeat this approach in the 4×4 matrix.

APPENDIX D: DYNAMICAL QUADRATIC FACTOR

Transmon-transmon pair: the ratio γ in Eq. (11) is around 1, so the perturbative dynamical quadratic factor η can be simplified as

$$
\eta = \frac{J_{01}^2}{2\delta\Delta^2(\delta - 2\Delta)(\delta - \Delta)^3(\delta + \Delta)^2}[8\delta^6 - 15\delta^5\Delta \\
- 18\delta^4\Delta^2 + 38\delta^3\Delta^3 + 6\delta^2\Delta^4 - \delta\Delta^5 + 2\Delta^6], \tag{D1}
$$

with $\delta_1 = \delta_2 = \delta$.

Transmon-CSFQ pair: the ratio γ in Eq. (11) is a slow changing parameter, approximately we can assume $\gamma = \gamma(\Delta = 0) \approx 3/2$, then η can be simplified as

$$
\eta = \frac{J_{01}^2}{16\delta\Delta^2(\delta + \Delta)(2\delta + \Delta)^3}[8\Delta^5 - 208\delta^5 \tag{D2}
$$

$$
- 472\delta^4\Delta - 304\delta^3\Delta^2 + 57\delta^2\Delta^3 + 97\delta\Delta^4]
$$

with $\delta_1 \approx -2\delta_2 = -2\delta$.

[1] R. Ayanzadeh, M. Halem, and T. Finin, Reinforcement quantum annealing: A hybrid quantum learning automata, Sci. Rep. **10**, 1 (2020).

[2] T. Brydges, A. Elben, P. Jurcevic, B. Vermersch, C. Maier, B. P. Lanyon, P. Zoller, R. Blatt, and C. F. Roos, Probing Rényi entanglement entropy via randomized measurements, Science **364**, 260 (2019).

[3] B. Foxen *et al.*, Demonstrating a Continuous set of Two-Qubit Gates for Near-Term Quantum Algorithms, Phys. Rev. Lett. **125**, 120504 (2020).

[4] F. Arute *et al.*, Quantum supremacy using a programmable superconducting processor, Nature **574**, 505 (2019).

[5] M. Kjaergaard, M. E. Schwartz, J. Braumüller, P. Krantz, J. I.-J. Wang, S. Gustavsson, and W. D. Oliver, Superconducting qubits: Current state of play, Annu. Rev. Condens. Matter Phys. **11**, 369 (2020).

[6] J. M. Martinis, M. H. Devoret, and J. Clarke, Quantum Josephson junction circuits and the dawn of artificial atoms, Nat. Phys. **16**, 234 (2020).

[7] R. C. Bialczak, M. Ansmann, M. Hofheinz, M. Lenander, E. Lucero, M. Neeley, A. D. O'Connell, D. Sank, H. Wang, M. Weides, J. Wenner, T. Yamamoto, A. N. Cleland, and J. M. Martinis, Fast Tunable Coupler for Superconducting Qubits, Phys. Rev. Lett. **106**, 060501 (2011).

[8] S. Gustavsson, F. Yan, G. Catelani, J. Bylander, A. Kamal, J. Birenbaum, D. Hover, D. Rosenberg, G. Samach, A. P. Sears, S. J. Weber, J. L. Yoder, J. Clarke, A. J. Kerman, F. Yoshihara, Y. Nakamura, T. P. Orlando, and W. D. Oliver, Suppressing relaxation in superconducting qubits by quasiparticle pumping, Science **354**, 1573 (2016).

[9] M. H. Ansari, Rate of tunneling nonequilibrium quasiparticles in superconducting qubits, Supercond. Sci. Technol. **28**, 045005 (2015).

[10] M. H. Ansari, F. K. Wilhelm, U. Sinha, and A. Sinha, The effect of environmental coupling on tunneling of quasiparticles in josephson junctions, Supercond. Sci. Technol. **26**, 125013 (2013).

[11] K. Serniak, M. Hays, G. de Lange, S. Diamond, S. Shankar, L. D. Burkhart, L. Frunzio, M. Houzet, and M. H. Devoret, Hot Nonequilibrium Quasiparticles in Transmon Qubits, Phys. Rev. Lett. **121**, 157701 (2018).

[12] M. H. Ansari and F. K. Wilhelm, Noise and microresonance of critical current in Josephson junction induced by Kondo trap states, Phys. Rev. B **84**, 235102 (2011).

[13] M. Bal, M. H. Ansari, J.-L. Orgiazzi, R. M. Lutchyn, and A. Lupascu, Dynamics of parametric fluctuations induced by quasiparticle tunneling in superconducting flux qubits, Phys. Rev. B **91**, 195434 (2015).

[14] P. Krantz, M. Kjaergaard, F. Yan, T. P. Orlando, S. Gustavsson, and W. D. Oliver, A quantum engineer's guide to superconducting qubits, Appl. Phys. Rev. **6**, 021318 (2019).

[15] S. A. Caldwell *et al.*, Parametrically Activated Entangling Gates Using Transmon Qubits, Phys. Rev. Appl. **10**, 034050 (2018).

[16] D. C. McKay, S. Filipp, A. Mezzacapo, E. Magesan, J. M. Chow, and J. M. Gambetta, Universal Gate for Fixed-Frequency Qubits via a Tunable bus, Phys. Rev. Appl. **6**, 064007 (2016).

[17] T. Walter, P. Kurpiers, S. Gasparinetti, P. Magnard, A. Potočnik, Y. Salathé, M. Pechal, M. Mondal, M. Oppliger, C. Eichler, and A. Wallraff, Rapid High-Fidelity Single-Shot Dispersive Readout of Superconducting Qubits, Phys. Rev. Appl. **7**, 054020 (2017).

[18] A. Blais, A. L. Grimsmo, S. Girvin, and A. Wallraff, Circuit quantum electrodynamics, arXiv:2005.12667.

[19] J. Ku, X. Xu, M. Brink, D. C. McKay, J. B. Hertzberg, M. H. Ansari, and B. L. T. Plourde, Suppression of Unwanted ZZ Interactions in a Hybrid Two-Qubit System, Phys. Rev. Lett. **125**, 200504 (2020).

[20] J. M. Chow, J. M. Gambetta, A. W. Cross, S. T. Merkel, C. Rigetti, and M. Steffen, Microwave-activated conditional-phase gate for superconducting qubits, New J. Phys. **15**, 115012 (2013).

[21] P. Mundada, G. Zhang, T. Hazard, and A. Houck, Suppression of Qubit Crosstalk in a Tunable Coupling Superconducting Circuit, Phys. Rev. Appl. **12**, 054023 (2019).

[22] D. C. McKay, S. Sheldon, J. A. Smolin, J. M. Chow, and J. M. Gambetta, Three-Qubit Randomized Benchmarking, Phys. Rev. Lett. **122**, 200502 (2019).

[23] S. Krinner, S. Lazar, A. Remm, C. K. Andersen, N. Lacroix, G. J. Norris, C. Hellings, M. Gabureac, C. Eichler, and A. Wallraff, Benchmarking Coherent Errors in Controlled-Phase Gates due to Spectator Qubits, Phys. Rev. Appl. **14**, 024042 (2020).

[24] P. Zhao, P. Xu, D. Lan, J. Chu, X. Tan, H. Yu, and Y. Yu, High-Contrast ZZ Interaction Using Superconducting Qubits with Opposite-Sign Anharmonicity, Phys. Rev. Lett. **125**, 200503 (2020).

[25] X. Li, T. Cai, H. Yan, Z. Wang, X. Pan, Y. Ma, W. Cai, J. Han, Z. Hua, X. Han, Y. Wu, H. Zhang, H. Wang, Y. Song, L. Duan, and L. Sun, Tunable Coupler for Realizing a Controlled-Phase Gate with Dynamically Decoupled Regime in a Superconducting Circuit, Phys. Rev. Appl. **14**, 024070 (2020).

[26] M. Malekakhlagh, E. Magesan, and D. C. McKay, First-principles analysis of cross-resonance gate operation, Phys. Rev. A **102**, 042605 (2020).

[27] C. Rigetti and M. Devoret, Fully microwave-tunable universal gates in superconducting qubits with linear couplings and fixed transition frequencies, Phys. Rev. B **81**, 134507 (2010).

[28] F. Yan, S. Gustavsson, A. Kamal, J. Birenbaum, A. P. Sears, D. Hover, T. J. Gudmundsen, D. Rosenberg, G. Samach, S. Weber, J. L. Yoder, T. P. Orlando, J. Clarke, A. J. Kerman, and W. D. Oliver, The flux qubit revisited to enhance coherence and reproducibility, Nat. Commun. **7**, 12964 (2016).

[29] J. Q. You, X. Hu, S. Ashhab, and F. Nori, Low-decoherence flux qubit, Phys. Rev. B **75**, 140515(R) (2007).

[30] M. Steffen, S. Kumar, D. P. DiVincenzo, J. R. Rozen, G. A. Keefe, M. B. Rothwell, and M. B. Ketchen, High-Coherence Hybrid Superconducting Qubit, Phys. Rev. Lett. **105**, 100502 (2010).

[31] N. Didier, E. A. Sete, M. P. da Silva, and C. Rigetti, Analytical modeling of parametrically modulated transmon qubits, Phys. Rev. A **97**, 022330 (2018).

[32] M. D. Reed, L. DiCarlo, S. E. Nigg, L. Sun, L. Frunzio, S. M. Girvin, and R. J. Schoelkopf, Realization of three-qubit quantum error correction with superconducting circuits, Nature **482**, 382 (2012).

[33] J. Koch, T. M. Yu, J. Gambetta, A. A. Houck, D. I. Schuster, J. Majer, A. Blais, M. H. Devoret, S. M. Girvin, and R. J. Schoelkopf, Charge-insensitive qubit design derived from the cooper pair box, Phys. Rev. A **76**, 042319 (2007).

[34] S. Bravyi, D. P. DiVincenzo, and D. Loss, Schrieffer–wolff transformation for quantum many-body systems, Ann. Phys. **326**, 2793 (2011).

[35] M. H. Ansari, Superconducting qubits beyond the dispersive regime, Phys. Rev. B **100**, 024509 (2019).

[36] L. S. Cederbaum, J. Schirmer, and H. D. Meyer, Block diagonalisation of hermitian matrices, J. Phys. A **22**, 2427 (1989).

[37] E. Magesan and J. M. Gambetta, Effective hamiltonian models of the cross-resonance gate, Phys. Rev. A **101**, 052308 (2020).

[38] M. H. Goerz, F. Motzoi, K. B. Whaley, and C. P. Koch, Charting the circuit qed design landscape using optimal control theory, npj Quantum Inf. **3**, 37 (2017).

[39] F. Yan, P. Krantz, Y. Sung, M. Kjaergaard, D. L. Campbell, T. P. Orlando, S. Gustavsson, and W. D. Oliver, Tunable Coupling Scheme for Implementing High-Fidelity Two-Qubit Gates, Phys. Rev. Appl. **10**, 054062 (2018).

[40] Y. Sung, L. Ding, J. Braumüller, A. Vepsäläinen, B. Kannan, M. Kjaergaard, A. Greene, G. O. Samach, C. McNally, D. Kim, A. Melville, B. M. Niedzielski, M. E. Schwartz, J. L. Yoder, T. P. Orlando, S. Gustavsson, and W. D. Oliver, Realization of high-fidelity CZ and ZZ-free iSWAP gates with a tunable coupler, arXiv:2011.01261.

[41] S. Krinner, P. Kurpiers, B. Royer, P. Magnard, I. Tsitsilin, J.-C. Besse, A. Remm, A. Blais, and A. Wallraff, Demonstration of an All-Microwave Controlled-Phase Gate between Far-Detuned Qubits, Phys. Rev. Appl. **14**, 044039 (2020).

[42] M. C. Collodo, J. Herrmann, N. Lacroix, C. K. Andersen, A. Remm, S. Lazar, J.-C. Besse, T. Walter, A. Wallraff, and C. Eichler, Implementation of Conditional Phase Gates Based on Tunable ZZ Interactions, Phys. Rev. Lett. **125**, 240502 (2020).

[43] Y. Xu, J. Chu, J. Yuan, J. Qiu, Y. Zhou, L. Zhang, X. Tan, Y. Yu, S. Liu, J. Li, F. Yan, and D. Yu, High-Fidelity, High-Scalability Two-Qubit Gate Scheme for Superconducting Qubits, Phys. Rev. Lett. **125**, 240503 (2020).

[44] S. Sheldon, E. Magesan, J. M. Chow, and J. M. Gambetta, Procedure for systematically tuning up cross-talk in the cross-resonance gate, Phys. Rev. A **93**, 060302(R) (2016).

[45] A. D. Córcoles, J. M. Gambetta, J. M. Chow, J. A. Smolin, M. Ware, J. Strand, B. L. T. Plourde, and M. Steffen, Process verification of two-qubit quantum gates by randomized benchmarking, Phys. Rev. A **87**, 030301(R) (2013).

[46] N. Sundaresan, I. Lauer, E. Pritchett, E. Magesan, P. Jurcevic, and J. M. Gambetta, Reducing unitary and spectator errors in cross resonance with optimized rotary echoes, PRX Quantum **1**, 020318 (2020).